Brief Communication

Cell Chemical Biology

A ZDHHC5-GOLGA7 Protein Acyltransferase Complex Promotes Nonapoptotic Cell Death

Graphical Abstract

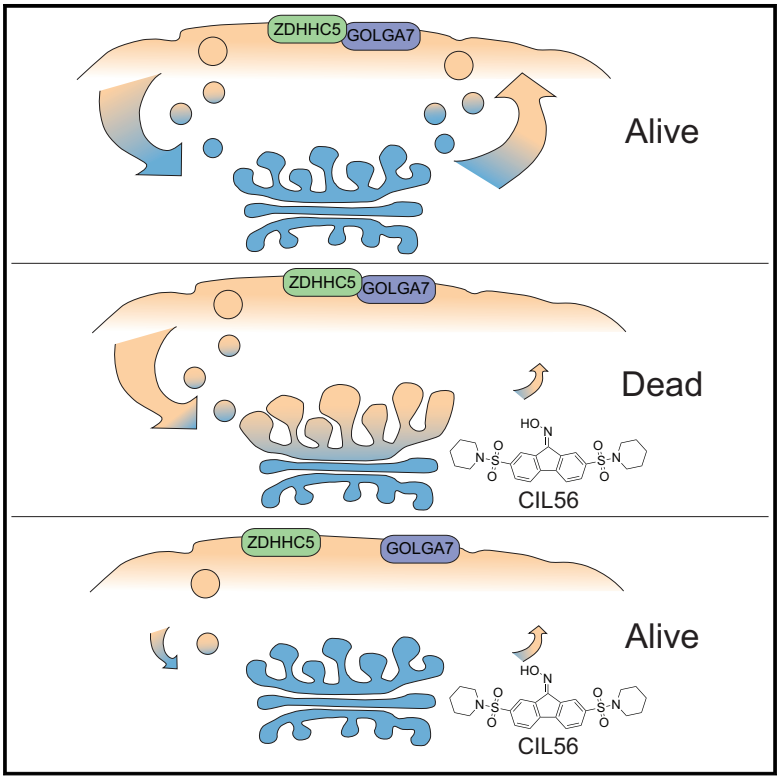

Highlights

- CIL56 triggers an unconventional form of nonapoptotic cell death
- Cell death requires protein acylation by a ZDHHC5-GOLGA7 complex
- CIL56 alters the structure of the Golgi apparatus and other organelles
- CIL56 and the ZDHHC5-GOLGA7 complex regulate membrane trafficking

Authors

Pin-Joe Ko, Claire Woodrow, Michael M. Dubreuil, Brent R. Martin, Rachid Skouta, Michael C. Bassik, Scott J. Dixon

Correspondence

sjdixon@stanford.edu

In Brief

CIL56 is a synthetic oxime that can trigger a form of nonapoptotic cell death that is distinct from apoptosis, necroptosis, ferroptosis, and classic necrosis. This unconventional form of cell death is promoted by a plasma membrane protein acyltransferase complex comprising ZDHHC5 and GOLGA7.

Ko et al., 2019, Cell Chemical Biology *26*, 1–9
December 19, 2019
https://doi.org/10.1016/j.chembiol.2019.09.014

CellPress

Please cite this article in press as: Ko et al., A ZDHHC5-GOLGA7 Protein Acyltransferase Complex Promotes Nonapoptotic Cell Death, Cell Chemical Biology (2019), https://doi.org/10.1016/j.chembiol.2019.09.014

Cell Chemical Biology
Brief Communication

A ZDHHC5-GOLGA7 Protein Acyltransferase Complex Promotes Nonapoptotic Cell Death

Pin-Joe Ko,[1] Claire Woodrow,[1] Michael M. Dubreuil,[2] Brent R. Martin,[3] Rachid Skouta,[4] Michael C. Bassik,[2] and Scott J. Dixon[1,5,*]
[1]Department of Biology, Stanford University, Stanford, CA 94305, USA
[2]Department of Genetics, Stanford University School of Medicine, Stanford, CA 94305, USA
[3]Department of Chemistry, University of Michigan, Ann Arbor, MI 48109, USA
[4]Department of Biology, University of Massachusetts Amherst, Amherst, MA 01003, USA
[5]Lead Contact
*Correspondence: sjdixon@stanford.edu
https://doi.org/10.1016/j.chembiol.2019.09.014

SUMMARY

Lethal small molecules are useful probes to discover and characterize novel cell death pathways and biochemical mechanisms. Here we report that the synthetic oxime-containing small molecule caspase-independent lethal 56 (CIL56) induces an unconventional form of nonapoptotic cell death distinct from necroptosis, ferroptosis, and other pathways. CIL56-induced cell death requires a catalytically active protein S-acyltransferase complex comprising the enzyme ZDHHC5 and an accessory subunit GOLGA7. The ZDHHC5-GOLGA7 complex is mutually stabilizing and localizes to the plasma membrane. CIL56 inhibits anterograde protein transport from the Golgi apparatus, which may be lethal in the context of ongoing ZDHHC5-GOLGA7 complex-dependent retrograde protein trafficking from the plasma membrane to internal sites. Other oxime-containing small molecules, structurally distinct from CIL56, may trigger cell death through the same pathway. These results define an unconventional form of nonapoptotic cell death regulated by protein S-acylation.

INTRODUCTION

Protein S-acylation, the thioesterification of a fatty acid to one or more internal cysteine residues of substrate proteins, regulates the membrane association, trafficking, stability, and function of hundreds of proteins in the cell (Ernst et al., 2018; Li et al., 2012; Linder and Deschenes, 2007). This modification is catalyzed in human cells by a family of 23 zinc finger DHHC domain-containing (ZDHHC) protein acyltransferases (PATs) that localize to the endoplasmic reticulum (ER), Golgi apparatus, and plasma membrane (Ko and Dixon, 2018; Ohno et al., 2006). Certain PATs require an accessory subunit to function. For example, ZDHHC9 binding to GOLGA7 is essential for the function of this PAT (Ohta et al., 2003; Swarthout et al., 2005). How accessory proteins promote PAT function, and whether they are shared between PATs, is not clear. More broadly, little is known about how PAT activity regulates cell fate.

Lethal small molecules can be used to discover and characterize cell death pathways, some of which may be clinically exploitable (Dixon et al., 2014; Li et al., 2017). CIL56 is a lethal compound with a poorly characterized mechanism of action that may have utility as an anti-cancer agent (Dixon et al., 2015; Shimada et al., 2016; Song et al., 2018). Mutation of *ACACA*, encoding the rate-limiting *de novo* fatty acid biosynthetic enzyme acetyl-coenzyme A (CoA) carboxylase 1 (ACC1), reduces sensitivity to CIL56 (Dixon et al., 2015). This suggests that fatty acid synthesis is required for CIL56 to induce cell death, but details of this lethal process are otherwise unknown. Here, we show that CIL56 promotes cell death through an unconventional mechanism distinct from apoptosis and several known nonapoptotic pathways. This mechanism requires a plasma membrane-localized PAT complex comprising ZDHHC5 and GOLGA7 and involves disruption of Golgi function and membrane trafficking. These results link PAT complex activity to the regulation of an unconventional form of nonapoptotic cell death.

RESULTS AND DISCUSSION

To better characterize the CIL56 lethal mechanism, we began by surveying the lethality of this compound in a panel of 94 human cell lines. Overall CIL56 inhibited cell viability in most cell types with 10–100 nM potency, with hematological cancers generally more sensitive, muscle and liver cancer cells less sensitive, and non-transformed peripheral blood mononuclear cells completely insensitive up to the maximum tested concentration (Figures 1A and 1B). Consistent with previous results (Dixon et al., 2015), CIL56-induced cell death was potently suppressed in several lineally distinct cell types, including HT-1080 fibrosarcoma cells, A549 non-small-cell lung carcinoma cells and T98G glioblastoma cells, by the ACC1 inhibitor 5-(tetradecyloxy)-2-furoic acid (TOFA) (Figures 1C, S1A, and S1B; see also below). CIL56-induced cell death was also prevented by triacsin C, which blocks the conversion of free fatty acids to fatty acyl-CoAs by long-chain acyl-CoA synthetases (Figure S1C). These results suggested that CIL56 triggered a generalizable form of regulated cell death in diverse cell types that required activated fatty acyl-CoAs.

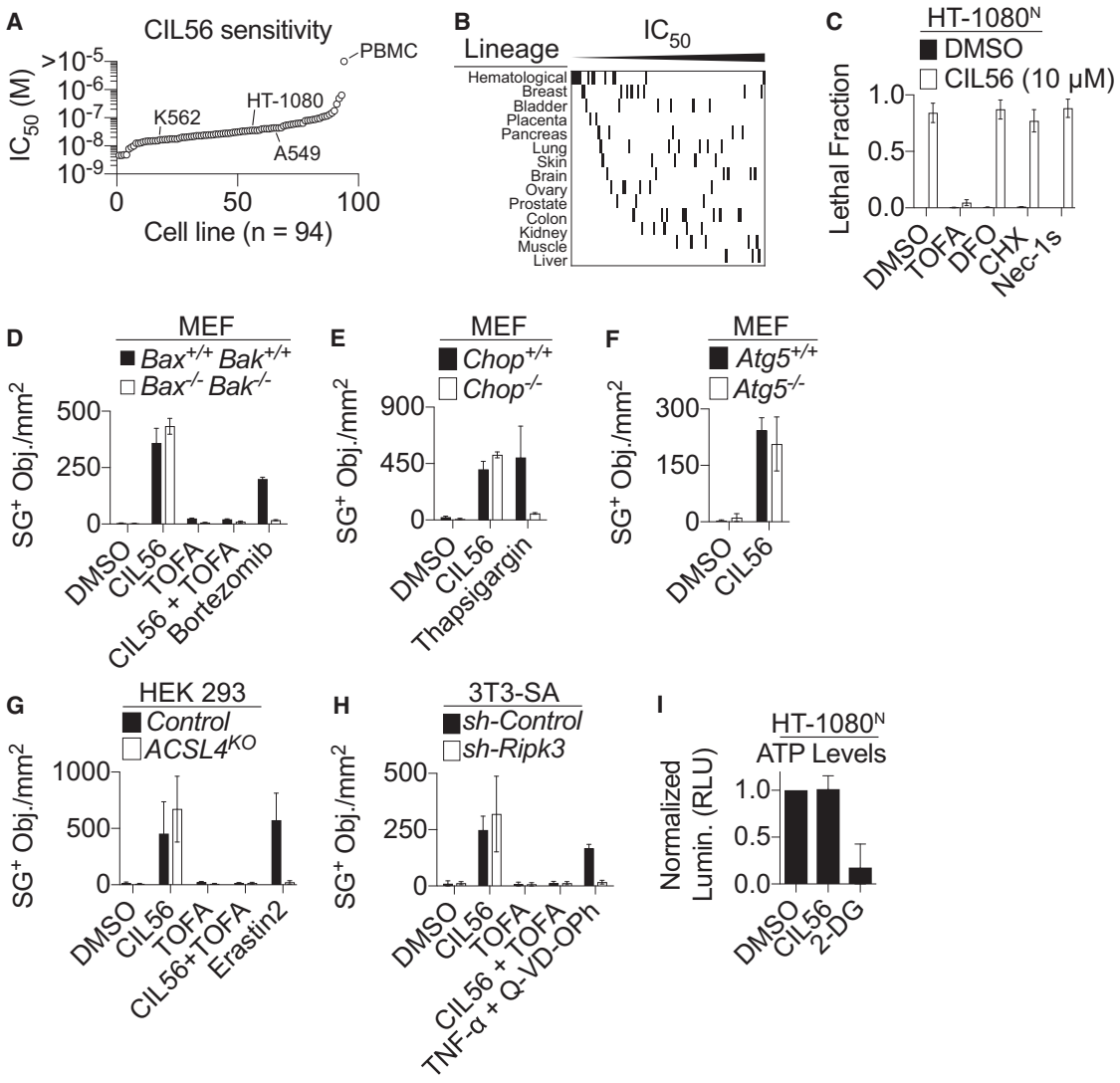

Figure 1. CIL56 Triggers an Unconventional Form of Cell Death

(A) CIL56 lethal potency in a panel of 94 cell lines. For peripheral blood mononuclear cells there was no observed lethality at the highest tested dose (10 μM).

(B) Relationship between CIL56 potency and cell lineage for a subset of cell lines tested in (A).

(C) Effect of inhibitors on CIL56-induced cell death in HT-1080 cells. These cells express the live cell marker nuclear-localized mKate2 (denoted as HT-1080^{N}). Cell death is presented as the lethal fraction (0 = all cells alive, 1 = all cells dead).

(D–F) SYTOX Green-positive (SG^{+}) dead cell counts at 24 h in paired control and genetically modified mouse embryonic fibroblasts (MEF) lacking *Bax* and *Bak* (D), *Chop* (E), or *Atg5* (F). Compound concentrations: CIL56 (10 μM), TOFA (1 μM), bortezomib (200 nM), and thapsigargin (100 nM). Bortezomib and thapsigargin are positive control inducers of apoptotic and ER stress-induced death, respectively.

(G) SG^{+} counts at 24 h ± CIL56 (5 μM) ± TOFA (1 μM). Erastin2 (1 μM, 48 h) is a positive control for the induction of ACSL4-dependent ferroptosis.

(H) SG^{+} counts at 24 h in infected cells ± CIL56 (10 μM) ± TOFA (1 μM). Tumor necrosis factor alpha (TNF-α) (10 ng/μL) + Q-VD-OPh (20 μM) is a positive control for the induction of Ripk3-dependent necroptosis.

(I) ATP levels in HT-1080^{N} cells treated for 6 h with vehicle control (DMSO), CIL56 (10 μM), or 2-deoxyglucose (2-DG) (50 mM). Assay luminescence was normalized to DMSO control. Data in (C–I) represent mean ± SD from three independent experiments.

We next examined whether CIL56 activated a known cell death pathway. Small-molecule inhibitors of caspase activity (Q-VD-OPh), lipid peroxidation (deferoxamine, ferrostatin-1), receptor interacting protein kinase 1 (necrostatin-1s), and protein synthesis (cycloheximide) had no effect on the lethality of CIL56 (Figures 1C, S1A, and S1B). CIL56 was lethal to immortalized mouse embryonic fibroblasts lacking the pro-apoptotic genes *Bax* and *Bak*, the ER stress-induced apoptosis regulator *Chop*, and the autophagy gene *Atg5* (Figures 1D–1F). CIL56 was also lethal to HEK293 cells lacking the pro-ferroptotic gene acyl-CoA synthetase long-chain family member 4 (*ACSL4*) (Dixon et al., 2015), and to murine 3T3-SA fibroblasts where expression of the necroptosis effector *Ripk3* was suppressed by short hairpin RNA (shRNA) (Kaiser et al., 2013) (Figures 1G and 1H). CIL56 treatment did not lower intracellular ATP levels over 6 h, inconsistent with direct membrane

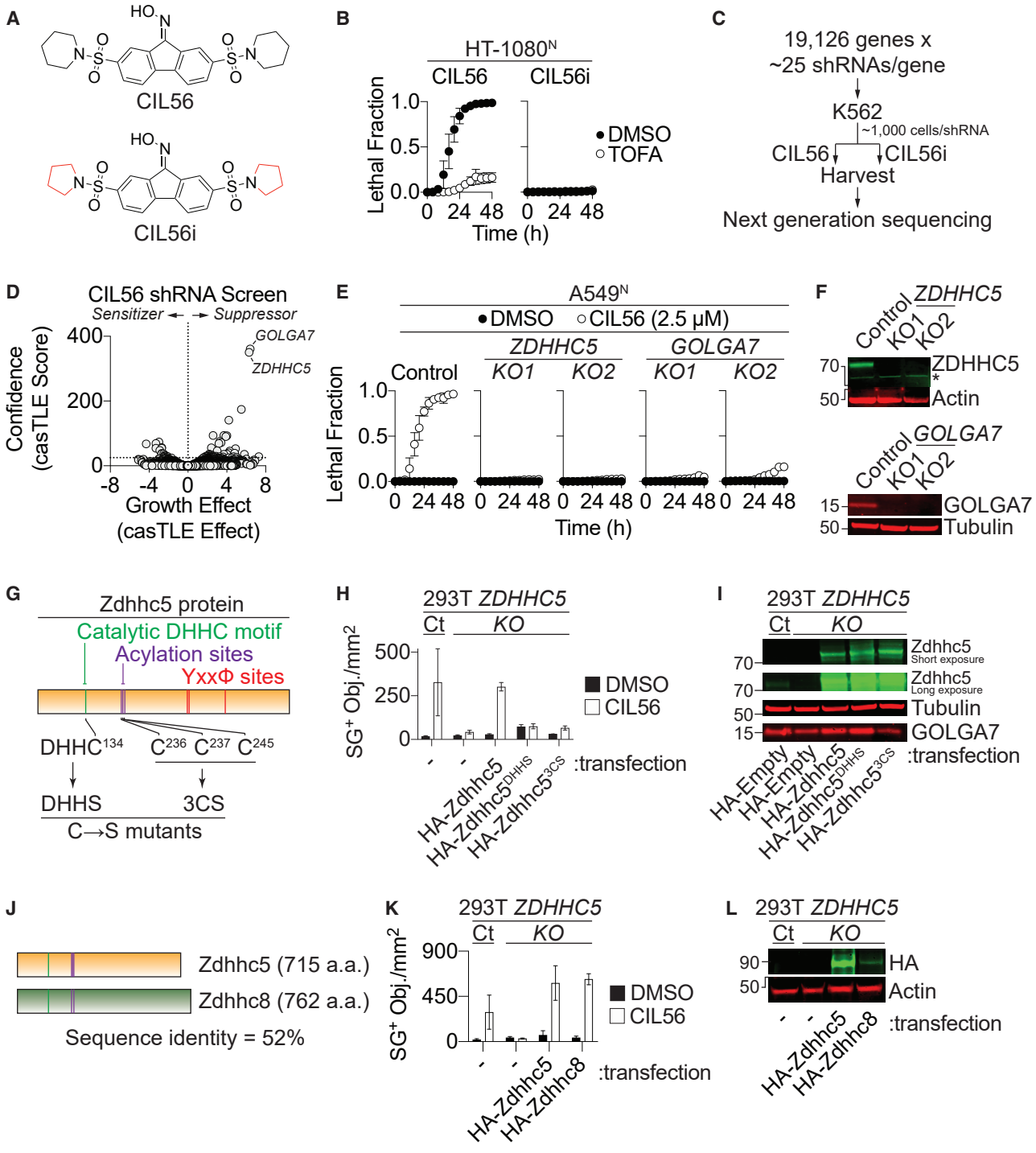

Figure 2. CIL56-Induced Cell Death Requires ZDHHC5 and GOLGA7

(A) Structures of CIL56 and an inactive analog, CIL56i.

(B) Cell death ± CIL56 or CIL56i (both 10 μM) ± TOFA (1 μM).

(C) Overview of the genetic screen in K562 cells. CIL56 and CIL56i were used at 1.25 μM.

(D) Results of the genetic screen pinpointing *GOLGA7* and *ZDHHC5*. The horizontal dotted line indicates the cutoff for statistical significance.

(E) Cell death in control or genetically modified A549^{N} cells.

(F) ZDHHC5 and GOLGA7 expression in gene-disrupted A549^{N} cells determined by western blotting. *Indicates non-specific band.

(G) Schematic of ZDHHC5 protein sequence. DHHS and 3CS mutants have cysteine-to-serine mutations in the catalytic residue and three Cys acylation sites, respectively.

(legend continued on next page)

permeabilization or a classic necrotic phenotype (Kushnareva and Newmeyer, 2010) (Figure 1I). Collectively, these results suggest that CIL56 triggered an unconventional form of cell death distinct from apoptosis, ferroptosis, necroptosis, and classic necrosis.

To gain more insight into the regulation of CIL56-induced cell death, we performed a genome-wide ultracomplex shRNA library screen in K562 leukemia cells (Kampmann et al., 2015), which we confirmed were sensitive to CIL56 in a TOFA-dependent manner (Figures 1A and S2A). Pools of shRNA library-infected K562 cells were treated over 12 days with 4 separate pulses of CIL56 or an inactive CIL56 analog we identified, termed CIL56i, in which pyrrolidines replace the piperidine rings of the parent compound (Figures 2A–2C, S2B, and S2C). Following genomic DNA isolation and deep sequencing, 18 candidate enhancer genes and 43 candidate suppressor genes were identified using an established statistical framework (Morgens et al., 2016) (Figures S2D and S2E). shRNAs targeting genes involved in fatty acid synthesis and activation (*FASN, ACACA*, and *ACSL3*) reduced sensitivity to CIL56, as expected from previous studies and results obtained with TOFA and triacsin C (Figures S2D and S1A–S1C) (Dixon et al., 2015). However, sensitivity to CIL56 was most strongly reduced by shRNAs targeting two genes involved in protein S-acylation: *ZDHHC5* and *GOLGA7* (Figures 2D and S2D). We confirmed that genetic disruption (hereafter knockout [KO]) of *ZDHHC5* or *GOLGA7* reduced sensitivity to CIL56 in $A549^{N}$, HT-1080, and HAP1 cells, indicating a generalizable requirement for both genes in promoting cell death (Figures 2E, 2F, and S2F–S2J).

Roles for protein S-acylation in nonapoptotic cell death are not well established. Therefore, we first examined the requirement for ZDHHC5 in CIL56-induced cell death. ZDHHC5 contains a catalytic cysteine (Cys) residue at position 134, three C-terminal acylated Cys residues of unknown function, and three YxxΦ clathrin-binding motifs likely involved in ZDHHC5 trafficking (Breusegem and Seaman, 2014; Brigidi et al., 2015; Yang et al., 2010). CIL56 sensitivity was restored in 293T $ZDHHC5^{KO}$ cells overexpressing wild-type mouse Zdhhc5 (98% identical to the human enzyme [Fukata et al., 2006]) or a Zdhhc5 mutant with tyrosine-to-alanine substitutions disrupting all three YxxΦ sites, but not in cells overexpressing a catalytically inactive mutant (DHHS) or a mutant where all three acylated Cys residues were mutated to serine (3CS) (Figures 2G–2I and S2K). Thus, CIL56-induced cell death requires ZDHHC5 catalytic activity and C-terminal acylation, but not interaction with clathrin. Of note, the close Zdhhc5 paralog Zdhhc8 also restored CIL56-induced cell death when overexpressed in 293T $ZDHHC5^{KO}$ cells (Figures 2J–2L). This is consistent with functional redundancy between these two enzymes observed in neurons (Thomas et al., 2012), and may explain why *ZDHHC5* disruption does not fully prevent CIL56-induced cell death in some cells (e.g., Figures S2G and S2J).

GOLGA7 is necessary for the stability and function of ZDHHC9 (Swarthout et al., 2005). However, *ZDHHC9* was not a hit in the shRNA screen (Figure S2D). Likewise, 293T cells lacking *ZDHHC9* remained sensitive to CIL56-induced death (Figures S3A–S3C). Interestingly, *ZDHHC5* and *GOLGA7* exhibited highly correlated genetic co-dependencies in a large compendium of CRISPR/Cas9 cancer cell fitness screens, suggesting a potential functional interaction (Meyers et al., 2017) (Figure 3A). This prompted us to test whether GOLGA7 could complex with ZDHHC5. Indeed, both ZDHHC5 and ZDHHC9 were recovered in anti-Flag immunoprecipitates from 293T cells expressing Flag-tagged GOLGA7 (Figures 3B and 3C). These interactions were abolished in cells expressing $GOLGA7^{2CS}$, a mutant that cannot be acylated on two cysteine residues essential for the function of this protein (Ohta et al., 2003) (Figures 3B and 3C). Functionally, overexpression in 293T $GOLGA7^{KO}$ cells of wild-type GOLGA7, but not $GOLGA7^{2CS}$, fully restored CIL56 sensitivity (Figures 3D and 3E). Thus, complex formation between ZDHHC5 and GOLGA7 appears necessary for CIL56 to promote cell death. Furthermore, as endogenous GOLGA7 was captured in immunoprecipitates from 293T cells transfected with wild-type Zdhhc5 and $Zdhhc5^{DHHS}$, but not $Zdhhc5^{3CS}$ (Figure 3F), we infer that ZDHHC5-GOLGA7 complex formation is independent of ZDHHC5 catalytic activity but dependent on ZDHHC5 C-terminal acylation.

To complement these biochemical studies, we examined the intracellular localization of ZDHHC5 and GOLGA7. Epitope-tagging and large-scale cell fractionation studies suggest that ZDHHC5 localizes to the plasma membrane (Ohta et al., 2003; Orre et al., 2019). Indeed, both wild-type Zdhhc5 and the catalytically inactive $Zdhhc5^{DHHS}$ mutant colocalized with the plasma membrane marker cadherin when expressed in HT-1080 $ZDHHC5^{KO1}$ cells, while the $Zdhhc5^{3CS}$ C-terminal Cys acylation mutant accumulated in cytosolic puncta (Figure S3D). C-terminal Cys acylation may therefore help target ZDHHC5 to the plasma membrane. GOLGA7 was initially reported to localize to the Golgi apparatus, but large-scale fractionation suggests that this protein may also be plasma membrane localized (Ohta et al., 2003; Orre et al., 2019). Consistent with these data, Flag-tagged GOLGA7 colocalized with endogenous ZDHHC5 at the plasma membrane of HT-1080 cells (Figure 3G). This colocalization appeared weaker in cells expressing the Flag-tagged $GOLGA7^{2CS}$ mutant, but not totally lost (Figure 3G). The membrane localization of wild-type GOLGA7 and $GOLGA7^{2CS}$ mutant was similar when these proteins were overexpressed in either control or $ZDHHC5^{KO1}$ cells (Figure 3G). Thus, neither GOLGA7 Cys acylation nor ZDHHC5 are absolutely essential for localization of GOLGA7 to the cell periphery. We find that GOLGA7 can also complex with ZDHHC8, another plasma membrane-localized PAT (Figure S3E) (Ohta et al., 2003; Orre et al., 2019). This interaction could help localize GOLGA7 to cell periphery in the absence of ZDHHC5 in some contexts. Nevertheless, substantially more wild-type GOLGA7 than $GOLGA7^{2CS}$ protein was detected in membrane fractions isolated from transfected 293T cells (Figure 3H). Loss of acylation in $GOLGA7^{2CS}$, as detected

(H) SG^{+} dead cell counts in control (Ct) and $ZDHHC5^{KO}$ 293T cells overexpressing the indicated proteins ± CIL56 (2.5 μM, 24 h).
(I) Western blot of Control (Ct) and $ZDHHC5^{KO}$ 293T cells overexpressing proteins as in (H).
(J) Comparison of Zdhhc5 and 8 protein sequences. Zdhhc8 is predicted to retain two of three acylated Cys residues found in Zdhhc5 (purple lines).
(K) SG^{+} dead cell counts in control (Ct) and $ZDHHC5^{KO}$ 293T cells overexpressing HA-Zdhhc5 or HA-Zdhhc8 ± CIL56 (2.5 μM, 24 h).
(L) Western blot of cells overexpressing proteins as in (K). Data in (B), (E), (H), and (K) are mean ± SD from three independent experiments.

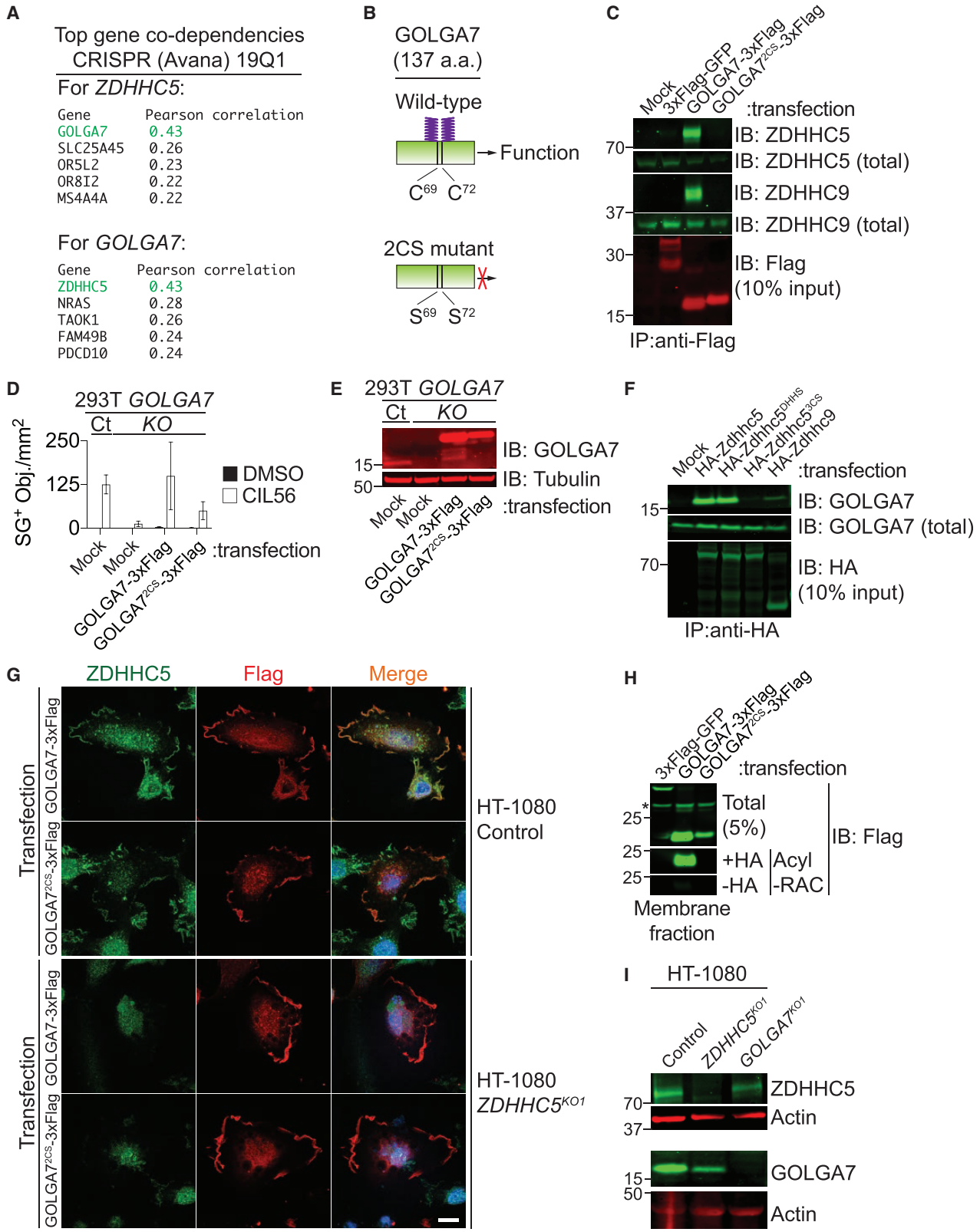

Figure 3. ZDHHC5 and GOLGA7 Form a Death-Promoting Complex

(A) Gene co-dependency lists for *ZDHHC5* and *GOLGA7* accessed from depmap.org.

(B) Schematic of GOLGA7 indicating the acylated cysteines required for function (Ohta et al., 2003). Cysteine 69 and 72 are mutated to serine in *GOLGA7*^{2CS}.

(legend continued on next page)

using acyl resin-assisted capture, likely weakens membrane association or reduce the stability of this protein, limiting complex formation at the plasma membrane with ZDHHC5 and other PATs (Figures 3H and S3F).

The role of accessory subunits in PAT regulation is poorly understood. In yeast, the GOLGA7 ortholog Erf4 promotes the stability of the ZDHHC9 ortholog Erf2 by shielding this protein from proteolytic degradation (Mitchell et al., 2012). Consistent with this observation, disruption of *GOLGA7* or *ZDHHC5* was associated with a reciprocal reduction in the levels of the other protein in both in HT-1080 and 293T cells (Figures 3I, S3B, and S3C). Furthermore, in 293T *ZDHHC5*^{KO} cells, endogenous GOLGA7 levels were stabilized by expression of wild-type Zdhhc5 or Zdhhc5^{DHHS}, which are capable of interacting with this protein, but not by expression of Zdhhc5^{3CS}, which cannot interact with GOLGA7 (Figure 2I). Thus, GOLGA7 and ZDHHC5 form a mutually stabilizing PAT complex that promotes cell death in response to CIL56 treatment.

Finally, we sought to link ZDHHC5-GOLGA7 complex function to the execution of nonapoptotic cell death in response to CIL56. We first determined that CIL56 treatment elicited a similar transcriptional response in Control and *ZDHHC5*^{KO} 293T cells, indicating that ZDHHC5 was not required for CIL56 uptake (Figure S4A). We next examined cell morphology using transmission electron microscopy, a classic means of studying cell death. CIL56 treatment altered mitochondrial morphology, disrupted the normally close apposition of mitochondria with the ER, and led to an accumulation of intracellular vesicles, all in a ZDHHC5-dependent manner (Figure 4A). We confirmed in live HT-1080 cells that CIL56 perturbed the gross structure of the mitochondrial and ER networks (Figures S4B and S4C). However, CIL56 did not reduce mitochondrial inner membrane transmembrane potential, alter cellular respiration, or cause transcriptional upregulation of canonical ER stress-associated genes (Figures S4A, S4D, and S4E). Thus, it seemed unlikely that altered mitochondrial or ER structure alone explained CIL56-induced cell death.

We next considered whether the accumulation of intracellular vesicles reflected a disruption of the Golgi apparatus, a major intracellular membrane trafficking hub. Strikingly, CIL56 treatment resulted in pronounced physical expansion of the Golgi apparatus (Figures 4B and 4C). This phenotype was specifically associated with dispersion of the *trans*-Golgi marker TGN46 away from the *cis*-Golgi marker GM130, as determined by immunofluorescence analysis, and required both ZDHHC5 and GOLGA7 (Figure 4D). ZDHHC5 promotes retrograde membrane trafficking from the plasma membrane and endosomes to the Golgi apparatus (Breusegem and Seaman, 2014; Sergeeva and van der Goot, 2019). We reasoned that ZDHHC5-dependent retrograde flux could lead to the observed physical expansion of the *trans*-Golgi and accumulation of intracellular vesicles if balancing anterograde transport from these sites to the plasma membrane was blocked by CIL56. Consistent with this possibility, CIL56 caused an accumulation of two classic plasma membrane-localized proteins, transferrin receptor (CD71) and epidermal growth factor receptor, within intracellular vesicle-like structures (Figure 4E). To examine anterograde membrane transport more directly, we used the retention using selective hooks system, where the anterograde movement of a reporter protein (tumor necrosis factor alpha fused to EGFP) through the secretory pathway can be selectively induced by the addition of biotin and monitored by time-lapse imaging (Boncompain et al., 2012). We added biotin and CIL56 at the same time to reporter-expressing cells and observed that CIL56 did not impair trafficking from the ER to the Golgi, but did result in greater retention of the reporter in the Golgi apparatus, an effect evident within 30 min of CIL56 addition (Figures 4F and 4G). Crucially, unlike other morphological and functional phenotypes, anterograde reporter protein transport was equally inhibited by CIL56 in both HT-1080 control and *ZDHHC5*^{KO1} cells, suggesting that this may be an early initiating event in the cell death cascade triggered by CIL56 (Figures 4F, 4G, and S4F).

We find that CIL56 triggers an unconventional form of nonapoptotic cell death in diverse cell types. We propose that inhibition of anterograde protein transport by CIL56, combined with ongoing ZDHHC5-GOLGA7 complex-dependent retrograde protein trafficking, leads to lethal protein mislocalization and accumulation within the cell. Disruption of ZDHHC5 slows retrograde protein transport (Breusegem and Seaman, 2014; Sergeeva and van der Goot, 2019; Thomas et al., 2012), potentially reducing lethal protein accumulation at the *trans*-Golgi and other sites within the cell when anterograde transport is blocked by CIL56. Whether the ZDHHC5-GOLGA7 complex promotes cell death by acylating specific transport substrates or by regulating the function of the retrograde transport machinery requires clarification. An intriguing possibility is that this trafficking-dependent lethal mechanism is related to the ZDHHC5-dependent massive endocytosis phenotype observed in cardiac muscle cells following anoxia/reoxygenation (Lin et al., 2013).

The specific molecular target(s) of CIL56 leading to cell death are unknown. Several otherwise structurally unrelated oxime-containing natural products are toxic to human cancer cells through unknown or partially characterized lethal mechanisms (Chen et al., 2016; Liu et al., 2016). Interestingly, the lethality of the synthetic oxime 7BIO, previously reported to trigger caspase-independent cell death (Ribas et al., 2006), was

(C) 293T cells overexpressing the indicated proteins and immunoprecipitated with Flag-conjugated magnetic beads, followed by western blotting as indicated.
(D) SG^{+} dead cell counts at 24 h for 293T control (Ct) or *GOLGA7*^{KO} cells expressing GOLGA7-3xFlag or GOLGA7^{2CS}-3xFlag ± CIL56 (2.5 μM, 24 h). Data are mean ± SD from three independent experiments.
(E) Western blot of 293T Control (Ct) and *GOLGA7*^{KO} cells expressing GOLGA7-3xFlag or GOLGA7^{2CS}-3xFlag.
(F) 293T cells expressing hemagglutinin (HA)-tagged Zdhhc5, Zdhhc5^{DHHS}, Zdhhc5^{3CS}, or Zdhhc9 and co-immunoprecipitated with HA-conjugated magnetic beads, followed by western blotting for endogenous GOLGA7.
(G) Confocal imaging of HT-1080 Control and *ZDHHC5*^{KO1} cells expressing GOLGA7-3xFlag or GOLGA7^{2CS}-3xFlag. Green, anti-ZDHHC5 (endogenous); red, anti-Flag; blue, DAPI. Scale bar, 15 μm.
(H) Western blot and acyl resin-assisted capture (RAC) analysis of the membrane fraction isolated from 293T cells following transfection with the indicated constructs. HA, hydroxylamine. *Indicates non-specific band.
(I) Western blot for endogenous ZDHHC5 and GOLGA7.

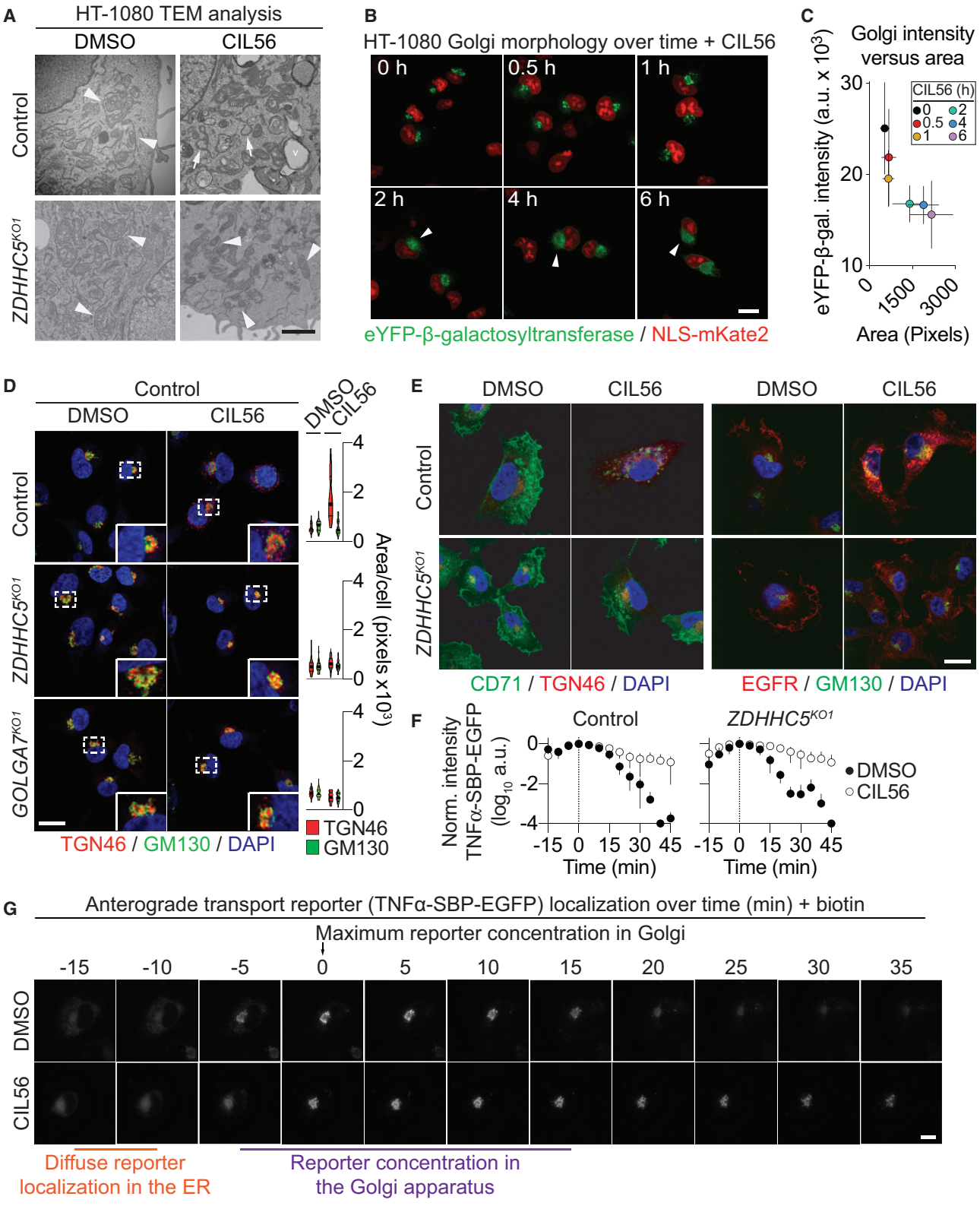

Figure 4. CIL56 Disrupts Golgi Structure and Function

(A) Transmission electron microscopy analysis of control and *ZDHHC5*^{KO1} HT-1080 cells ± CIL56 (2.5 μM, 4 h). Arrowheads indicate regions of close apposition between mitochondria and ER. Arrows indicate regions of ER that are no longer in close apposition to mitochondria. The lowercase "v" indicates vesicles. Scale bar, 2 μm.

(legend continued on next page)

suppressed by deletion of *ZDHHC5* (Figures S4G and S4H). Thus, structurally diverse oxime-containing molecules may trigger a common nonapoptotic cell death process that depends on protein S-acylation.

SIGNIFICANCE

Small molecule probes can facilitate the discovery and characterization of new cell death processes. We find that the synthetic small molecule CIL56 is capable of triggering an unconventional form of cell death in a wide range of mammalian cells that involves alterations in membrane trafficking and organization. This process is distinct from apoptosis, necroptosis, ferroptosis, and classic necrosis, and requires a PAT complex comprising ZDHHC5 and GOLGA7. The ZDHHC5-GOLGA7 PAT complex localizes to the plasma membrane, where it controls membrane trafficking events that may be lethal in cells treated with CIL56 or other oxime-containing compounds. It may be possible to harness this form of cell death to kill certain cancer cells. CIL56 also emerges as a probe that will be useful to define the function of the ZDHHC5-GOLGA7 complex in the cell.

STAR★METHODS

Detailed methods are provided in the online version of this paper and include the following:

- KEY RESOURCES TABLE
- LEAD CONTACT FOR MATERIALS AVAILABILITY
- EXPERIMENTAL MODEL AND SUBJECT DETAILS
  - Cell Lines and Culture Conditions
  - Chemicals and Reagents
- METHOD DETAILS
  - Cell Line Panel CIL56 Sensitivity Study
  - Cell Death Assessment Using STACK
  - CIL56 Structure Activity Relationship Analysis
  - Genome-wide shRNA Screen
  - CRISPR/Cas9 Gene Editing
  - ZDHHC and GOLGA7 Biochemistry
  - Immunoblotting
  - Acyl Resin-Assisted Capture
  - Confocal Immunofluorescence Imaging
  - Transmission Electron Microscopy
  - Mitochondria and ER Morphological and Functional Assessment
  - Golgi Imaging and RUSH Analysis
  - RNA Sequencing Analysis
- QUANTIFICATION AND STATISTICAL ANALYSIS
- DATA AND CODE AVAILABILITY

SUPPLEMENTAL INFORMATION

Supplemental Information can be found online at https://doi.org/10.1016/j.chembiol.2019.09.014.

ACKNOWLEDGMENTS

We thank Z. Inde, G. Forcina, and D. Morgens for experimental assistance, L. Magtanong for comments, T. Stearns for access to equipment and advice, J. Carette, A. Gitler, M. Fukata (National Institute for Physiological Sciences, Japan), and A-C. Gingras (Mount Sinai Hospital, Canada) for plasmids, and J. Olzmann (UC Berkeley) and W. Kaiser (UT Health San Antonio) for cell lines. This work was supported by an NIH training grant (T32 GM007276) to P.-J.K. and a Damon Runyon-Rachleff Innovation award to S.J.D.

AUTHOR CONTRIBUTIONS

Conceptualization, P.-J.K. and S.J.D.; Methodology, P.-J.K., C.W., and M.M.D.; Investigation, P.-J.K. and C.W.; Writing – Original Draft, P.-J.K. and S.J.D.; Writing – Review & Editing, P.-J.K., B.R.M., R.S., and S.J.D.; Resources, B.R.M., R.S., and M.C.B.; Supervision, M.C.B. and S.J.D.

DECLARATION OF INTERESTS

S.J.D. is a member of the scientific advisory board of Ferro Therapeutics.

Received: June 5, 2019
Revised: August 29, 2019
Accepted: September 26, 2019
Published: October 17, 2019

REFERENCES

Boncompain, G., Divoux, S., Gareil, N., de Forges, H., Lescure, A., Latreche, L., Mercanti, V., Jollivet, F., Raposo, G., and Perez, F. (2012). Synchronization of secretory protein traffic in populations of cells. Nat. Methods *9*, 493–498.

Breusegem, S.Y., and Seaman, M.N.J. (2014). Genome-wide RNAi screen reveals a role for multipass membrane proteins in endosome-to-Golgi retrieval. Cell Rep. *9*, 1931–1945.

Brigidi, G.S., Santyr, B., Shimell, J., Jovellar, B., and Bamji, S.X. (2015). Activity-regulated trafficking of the palmitoyl-acyl transferase DHHC5. Nat. Commun. *6*, 8200.

Chen, H.-P., Zhao, Z.-Z., Li, Z.-H., Dong, Z.-J., Wei, K., Bai, X., Zhang, L., Wen, C.-N., Feng, T., and Liu, J.-K. (2016). Novel natural oximes and oxime esters with a vibralactone backbone from the basidiomycete *Boreostereum vibrans*. ChemistryOpen *5*, 142–149.

Couzens, A.L., Knight, J.D.R., Kean, M.J., Teo, G., Weiss, A., Dunham, W.H., Lin, Z.-Y., Bagshaw, R.D., Sicheri, F., Pawson, T., et al. (2013). Protein interaction network of the mammalian Hippo pathway reveals mechanisms of kinase-phosphatase interactions. Sci. Signal. *6*, rs15.

(B) Imaging of the Golgi marker eYFP-β-galactosyltransferase in live cells over time. CIL56, 10 μM. Arrowheads point to enlarging Golgi structures. Scale bar, 15 μm.
(C) Quantification of Golgi size, as inferred from eYFP-β-galactosyltransferase (β-gal.) mean intensity and area measurements of cells treated as in (B). Eighteen to 30 cells were analyzed per time point.
(D) Immunofluorescence analysis of control and *ZDHHC5*^{KO1} HT-1080 cells fixed and stained for markers of the *trans*-Golgi (TGN46) or *cis*-Golgi (GM130). DAPI stains DNA. Scale bar, 20 μm. Quantification of Golgi marker pixel area is shown at right of the images. n > 45 cells/condition.
(E) Immunofluorescence of CD71 and epidermal growth factor receptor (EGFR) in HT-1080 cells ± CIL56 (2.5 μM, 4 h). Scale bar, 20 μm.
(F and G) Analysis of protein secretion with the retention using selective hooks (RUSH) system. HT-1080 Control and *ZDHHC5*^{KO1} cells transiently overexpressing the anterograde transport reporter TNFα-SBP-EGFP were incubated with biotin to release the reporter from an endoplasmic reticulum (ER)-localized "hook" protein ± CIL56 (2.5 μM) and then imaged every 5 min. In (F), TNF-α-SBP-EGFP intensity is quantified (mean ± SD) for five cells per condition. (G) Representative images of the reporter over time. Scale bar, 20 μm.

Deans, R.M., Morgens, D.W., Ökesli, A., Pillay, S., Horlbeck, M.A., Kampmann, M., Gilbert, L.A., Li, A., Mateo, R., Smith, M., et al. (2016). Parallel shRNA and CRISPR-Cas9 screens enable antiviral drug target identification. Nat. Chem. Biol. *12*, 361–366.

Dixon, S.J., Patel, D.N., Welsch, M., Skouta, R., Lee, E.D., Hayano, M., Thomas, A.G., Gleason, C.E., Tatonetti, N.P., Slusher, B.S., et al. (2014). Pharmacological inhibition of cystine-glutamate exchange induces endoplasmic reticulum stress and ferroptosis. Elife *3*, e02523.

Dixon, S.J., Winter, G.E., Musavi, L.S., Lee, E.D., Snijder, B., Rebsamen, M., Superti-Furga, G., and Stockwell, B.R. (2015). Human haploid cell genetics reveals roles for lipid metabolism genes in nonapoptotic cell death. ACS Chem. Biol. *10*, 1604–1609.

Ernst, A.M., Syed, S.A., Zaki, O., Bottanelli, F., Zheng, H., Hacke, M., Xi, Z., Rivera-Molina, F., Graham, M., Rebane, A.A., et al. (2018). S-Palmitoylation sorts membrane cargo for anterograde transport in the Golgi. Dev. Cell *47*, 479–493.e7.

Forcina, G.C., Conlon, M., Wells, A., Cao, J.Y., and Dixon, S.J. (2017). Systematic quantification of population cell death kinetics in mammalian cells. Cell Syst. *4*, 600–610.

Fukata, Y., Iwanaga, T., and Fukata, M. (2006). Systematic screening for palmitoyl transferase activity of the DHHC protein family in mammalian cells. Methods *40*, 177–182.

Goedhart, J., Stetten, von, D., Noirclerc-Savoye, M., Lelimousin, M., Joosen, L., Hink, M.A., van Weeren, L., Gadella, T.W.J., and Royant, A. (2012). Structure-guided evolution of cyan fluorescent proteins towards a quantum yield of 93%. Nat. Commun. *3*, 751.

Kaiser, W.J., Sridharan, H., Huang, C., Mandal, P., Upton, J.W., Gough, P.J., Sehon, C.A., Marquis, R.W., Bertin, J., and Mocarski, E.S. (2013). Toll-like receptor 3-mediated necrosis via TRIF, RIP3, and MLKL. J. Biol. Chem. *288*, 31268–31279.

Kampmann, M., Horlbeck, M.A., Chen, Y., Tsai, J.C., Bassik, M.C., Gilbert, L.A., Villalta, J.E., Kwon, S.C., Chang, H., Kim, V.N., et al. (2015). Next-generation libraries for robust RNA interference-based genome-wide screens. Proc. Natl. Acad. Sci. U S A *112*, E3384–E3391.

Ko, P.-J., and Dixon, S.J. (2018). Protein palmitoylation and cancer. EMBO Rep. *19*, e46666.

Kushnareva, Y., and Newmeyer, D.D. (2010). Bioenergetics and cell death. Ann. N. Y. Acad. Sci. *1201*, 50–57.

Li, Y., Martin, B.R., Cravatt, B.F., and Hofmann, S.L. (2012). DHHC5 protein palmitoylates flotillin-2 and is rapidly degraded on induction of neuronal differentiation in cultured cells. J. Biol. Chem. *287*, 523–530.

Li, Y., Qian, L., and Yuan, J. (2017). Small molecule probes for cellular death machines. Curr. Opin. Chem. Biol. *39*, 74–82.

Lin, M.-J., Fine, M., Lu, J.-Y., Hofmann, S.L., Frazier, G., and Hilgemann, D.W. (2013). Massive palmitoylation-dependent endocytosis during reoxygenation of anoxic cardiac muscle. Elife *2*, e01295.

Linder, M.E., and Deschenes, R.J. (2007). Palmitoylation: policing protein stability and traffic. Nat. Rev. Mol. Cell Biol. *8*, 74–84.

Liu, N., Song, L., Liu, M., Shang, F., Anderson, Z., Fox, D.J., Challis, G.L., and Huang, Y. (2016). Unique post-translational oxime formation in the biosynthesis of the azolemycin complex of novel ribosomal peptides from *Streptomyces* sp. FXJ1.264. Chem. Sci. *7*, 482–488.

Magtanong, L., Ko, P.-J., To, M., Cao, J.Y., Forcina, G.C., Tarangelo, A., Ward, C.C., Cho, K., Patti, G.J., Nomura, D.K., et al. (2019). Exogenous monounsaturated fatty acids promote a ferroptosis-resistant cell state. Cell Chem. Biol. *26*, 420–432.

Mandal, P., Berger, S.B., Pillay, S., Moriwaki, K., Huang, C., Guo, H., Lich, J.D., Finger, J., Kasparcova, V., Votta, B., et al. (2014). RIP3 induces apoptosis independent of pronecrotic kinase activity. Mol. Cell *56*, 481–495.

Meyers, R.M., Bryan, J.G., McFarland, J.M., Weir, B.A., Sizemore, A.E., Xu, H., Dharia, N.V., Montgomery, P.G., Cowley, G.S., Pantel, S., et al. (2017). Computational correction of copy number effect improves specificity of CRISPR-Cas9 essentiality screens in cancer cells. Nat. Genet. *49*, 1779–1784.

Mitchell, D.A., Hamel, L.D., Ishizuka, K., Mitchell, G., Schaefer, L.M., and Deschenes, R.J. (2012). The Erf4 subunit of the yeast Ras palmitoyl acyltransferase is required for stability of the Acyl-Erf2 intermediate and palmitoyl transfer to a Ras2 substrate. J. Biol. Chem. *287*, 34337–34348.

Morgens, D.W., Deans, R.M., Li, A., and Bassik, M.C. (2016). Systematic comparison of CRISPR/Cas9 and RNAi screens for essential genes. Nat. Biotechnol. *34*, 634–636.

Ohno, Y., Kihara, A., Sano, T., and Igarashi, Y. (2006). Intracellular localization and tissue-specific distribution of human and yeast DHHC cysteine-rich domain-containing proteins. Biochim. Biophys. Acta *1761*, 474–483.

Ohta, E., Misumi, Y., Sohda, M., Fujiwara, T., Yano, A., and Ikehara, Y. (2003). Identification and characterization of GCP16, a novel acylated Golgi protein that interacts with GCP170. J. Biol. Chem. *278*, 51957–51967.

Olenych, S.G., Claxton, N.S., Ottenberg, G.K., and Davidson, M.W. (2007). The fluorescent protein color palette. Curr. Protoc. Cell Biol., Chapter 21, Unit 21.5.

Orre, L.M., Vesterlund, M., Pan, Y., Arslan, T., Zhu, Y., Fernandez Woodbridge, A., Frings, O., Fredlund, E., and Lehtiö, J. (2019). SubCellBarCode: proteome-wide mapping of protein localization and relocalization. Mol. Cell *73*, 166–182.e7.

Ran, F.A., Hsu, P.D., Wright, J., Agarwala, V., Scott, D.A., and Zhang, F. (2013). Genome engineering using the CRISPR-Cas9 system. Nat. Protoc. *8*, 2281–2308.

Ribas, J., Bettayeb, K., Ferandin, Y., Knockaert, M., Garrofé-Ochoa, X., Totzke, F., Schächtele, C., Mester, J., Polychronopoulos, P., Magiatis, P., et al. (2006). 7-Bromoindirubin-3'-oxime induces caspase-independent cell death. Oncogene *25*, 6304–6318.

Sergeeva, O.A., and van der Goot, F.G. (2019). Anthrax toxin requires ZDHHC5-mediated palmitoylation of its surface-processing host enzymes. Proc. Natl. Acad. Sci. U S A *116*, 1279–1288.

Shimada, K., Skouta, R., Kaplan, A., Yang, W.S., Hayano, M., Dixon, S.J., Brown, L.M., Valenzuela, C.A., Wolpaw, A.J., and Stockwell, B.R. (2016). Global survey of cell death mechanisms reveals metabolic regulation of ferroptosis. Nat. Chem. Biol. *12*, 497–503.

Song, S., Xie, M., Scott, A.W., Jin, J., Ma, L., Dong, X., Skinner, H.D., Johnson, R.L., Ding, S., and Ajani, J.A. (2018). A novel YAP1 inhibitor targets CSC-enriched radiation-resistant cells and exerts strong antitumor activity in esophageal adenocarcinoma. Mol. Cancer Ther. *17*, 443–454.

Swarthout, J.T., Lobo, S., Farh, L., Croke, M.R., Greentree, W.K., Deschenes, R.J., and Linder, M.E. (2005). DHHC9 and GCP16 constitute a human protein fatty acyltransferase with specificity for H- and N-Ras. J. Biol. Chem. *280*, 31141–31148.

Thomas, G.M., Hayashi, T., Chiu, S.-L., Chen, C.-M., and Huganir, R.L. (2012). Palmitoylation by DHHC5/8 targets GRIP1 to dendritic endosomes to regulate AMPA-R trafficking. Neuron *73*, 482–496.

Yang, W., Di Vizio, D., Kirchner, M., Steen, H., and Freeman, M.R. (2010). Proteome scale characterization of human S-acylated proteins in lipid raft-enriched and non-raft membranes. Mol. Cell. Proteomics *9*, 54–70.

STAR★METHODS

KEY RESOURCES TABLE

REAGENT or RESOURCE	SOURCE	IDENTIFIER
Antibodies		
Rabbit α-ZDHHC5	Sigma-Aldrich	Cat# HPA014670; RRID:AB_2257442
Rabbit α-ZDHHC9	Novus Biologicals	Cat# NBP1-84499; RRID:AB_11010738
Mouse α-GOLGA7	Novus Biologicals	Cat# H00051125-M01; RRID:AB_2279239
Goat α-FLAG	Abcam	Cat# ab1257; RRID:AB_299216
Mouse α-HA	Biolegend	Cat# 901502; RRID:AB_2565007
Rabbit α-HA	Cell Signaling Technology	Cat# 3724; RRID:AB_1549585
Mouse α-GM130	BD Biosciences	Cat# 610822; RRID:AB_398141
Rabbit α-TGN46	Novus Biologicals	Cat# NBP1-49643; RRID:AB_10011762
Mouse α-tubulin	Millipore Sigma	Cat# MS-581; RRID:AB_144075
Goat α-actin	Santa Cruz Biotechnology	Cat# sc-1616; RRID:AB_630836
Mouse α-actin	Santa Cruz Biotechnology	Cat# sc-47778; RRID:AB_2714189
Rabbit α-EGFR	Cell Signaling Technology	Cat# 6627; RRID:AB_10692501
Mouse α-CD71	BioXCell	Cat# BE0023; RRID:AB_1107669
Goat polyclonal anti-rabbit Highly Cross-Adsorbed Secondary Antibody, Alexa Fluor 568	Life Technologies	Cat# A11036; RRID:AB_143011
Goat polyclonal anti-mouse Highly Cross-Adsorbed Secondary Antibody, Alexa Fluor 488	Life Technologies	Cat# A11029; RRID:AB_138404
Donkey polyclonal anti-goat Highly Cross-Adsorbed Secondary Antibody, Alexa Fluor 568	Life Technologies	Cat# A11057; RRID:AB_142581
Donkey polyclonal anti-rabbit Highly Cross-Adsorbed Secondary Antibody, Alexa Fluor 488	Life Technologies	Cat# A21206; RRID:AB_2535792
Bacterial and Virus Strains		
IncuCyte™ NucLight™ Red Lentivirus Reagent (EF-1α, Puro)	Essen BioScience	Cat# 4625
Chemicals, Peptides, and Recombinant Proteins		
CIL56	Acme Bioscience	N/A
Erastin2 (Compound 35MEW28 in Dixon et al., 2014)	Dixon et al., 2014	N/A
SYTOX Green	Life Technologies	Cat# S7020
Dimethyl sulfoxide	Sigma-Aldrich	Cat# 276855; CAS: 67-68-5
5-(Tetradecyloxy)-2 furoic acid	Sigma-Aldrich	Cat# T6575
Thapsigargin	Sigma-Aldrich	Cat# T9033; CAS: 67526-95-8
Staurosporine	Sigma-Aldrich	Cat# S6942
Cycloheximide	Sigma-Aldrich	Cat# C7698
2-deoxy-D-glucose	Sigma-Aldrich	Cat# D8375
Ferrostatin-1	Sigma-Aldrich	Cat# SML0583; CAS: 347174-05-4
FCCP	Cayman Chemicals	Cat# 15218
Necrostatin-1s	BioVision	Cat# 2263
Bortezomib	Fisher Scientific	Cat# NC0587961; CAS: 179324-69-7
Q-VD-OPh	Fisher Scientific	Cat# OPH00101M

(*Continued on next page*)

Continued

REAGENT or RESOURCE	SOURCE	IDENTIFIER
Triacsin C	Cayman Chemicals	Cat# 10007448
9-oxo-9H-fluorene-2,7-disulfonyl dichloride (Compound 2)	Sigma Aldrich	Cat# CDS013683
1509-0124 (Compound 3)	ChemDiv	1509-0124
5267-1376 (Compound 4, CIL56i)	ChemDiv	5267-1376
4345-0010 (Compound 5)	ChemDiv	4345-0010
1869-0039 (Compound 6)	ChemDiv	1869-0039
1509-0058 (Compound 7)	ChemDiv	1509-0058
1869-0197 (Compound 8)	ChemDiv	1869-0197
Critical Commercial Assays		
Pierce Microplate BCA Protein Assay Kit	Thermo Fisher Scientific	Cat# 23252
Deposited Data		
RNA sequencing data for 293T Control and ZDHHC5KO cells treated ± CIL56 (2.5 μM, 1 h)	This paper	https://data.mendeley.com/datasets/m6fp39vyd9/1
Experimental Models: Cell Lines		
Human: HT-1080	ATCC	CCL-121
Mouse: DR-Wildtype	ATCC	CRL-2977
Mouse: CHOP-KO-DR	ATCC	CRL-2979
Mouse: ATG5$^{+/+}$ MEF	RIKEN BRC Cell Bank	RCB2710
Mouse: ATG5$^{-/-}$ MEF	RIKEN BRC Cell Bank	RCB2711
Human: HT-1080^{N}	Forcina et al., 2017	N/A
Human: A549^{N}	Forcina et al., 2017	N/A
Human: T98G^{N}	Forcina et al., 2017	N/A
Mouse: 3T3-SA scr-shRNA	Mandal et al., 2014	N/A
Mouse: 3T3-SA Ripk3 KD	Mandal et al., 2014	N/A
Mouse: WT SV40 MEF	ATCC	CRL-2907
Mouse: Bax Bak DKO SV40 MEF	ATCC	CRL-2913
Human: HAP1 Control	Horizon Discovery	Cat# C631
Human: HAP1 *ZDHHC5*^{KO}	Horizon Discovery	Cat# HZGHC000589c012
Human: HEK 293 Control	Magtanong et al., 2019	N/A
Human: HEK 293 *ACSL4*^{KO}	Magtanong et al., 2019	N/A
Human: HEK-293T	ATCC	CRL-3216
Human: HEK-293T Control	This paper	N/A
Human: HEK-293T *ZDHHC5*^{KO}	This paper	N/A
Human: HEK-293T *GOLGA7*^{KO}	This paper	N/A
Human: HEK-293T *ZDHHC9*^{KO}	This paper	N/A
Human: HT-1080 Control	This paper	N/A
Human: HT-1080 *ZDHHC5*^{KO1}	This paper	N/A
Human: HT-1080 *ZDHHC5*^{KO2}	This paper	N/A
Human: HT-1080 *GOLGA7*^{KO}	This paper	N/A
Human: HT-1080 *ZDHHC9*^{KO}	This paper	N/A
Human: HT-1080^{N} *ZDHHC5*^{KO1}	This paper	N/A
Human: HT-1080^{N} *GOLGA7*^{KO}	This paper	N/A
Human: HT-1080^{N} *ZDHHC9*^{KO}	This paper	N/A
Human: A549^{N} Control	This paper	N/A
Human: A549^{N} *ZDHHC5*^{KO}	This paper	N/A
Human: A549^{N} *GOLGA7*^{KO}	This paper	N/A

(*Continued on next page*)

Continued

REAGENT or RESOURCE	SOURCE	IDENTIFIER
Oligonucleotides		
See Table S1.		
Recombinant DNA		
pmTurquoise2-Mito	Goedhart et al., 2012	Addgene #36208; RRID:Addgene_36208
pmTurquoise2-ER	Goedhart et al., 2012	Addgene #36204; RRID:Addgene_36204
EYFP-Golgi-7	Olenych et al., 2007	Addgene #56590; RRID:Addgene_56590
Str-KDEL_TNF-SBP-EGFP	Boncompain et al., 2012	Addgene #65278; RRID:Addgene_65278
pSpCas9(BB)-2A-GFP	Ran et al., 2013	Addgene #48138; RRID:Addgene_48138
pSpCas9(BB)-2A-GFP-sgRNA-ZDHHC5	This paper	N/A
pSpCas9(BB)-2A-GFP-sgRNA-GOLGA7	This paper	N/A
pEF-BOS-HA	Fukata et al., 2006	N/A
pEF-BOS-HA-Zdhhc5	Fukata et al., 2006	N/A
pEF-BOS-HA-Zdhhc9	Fukata et al., 2006	N/A
pEF-BOS-HA-Zdhhc2	Fukata et al., 2006	N/A
pEF-BOS-HA-Zdhhc8	Fukata et al., 2006	N/A
pEF-BOS-HA-Zdhhc5-C134S	This paper	N/A
pEF-BOS-HA-Zdhhc5-C236,237,245S	This paper	N/A
pEF-BOS-HA-Zdhhc5-Y456,470,533A	This paper	N/A
pDEST-pcDNA5-FLAG C-term	Couzens et al., 2013	N/A
pCDNA5-Nterm-FLAG-eGFP	This paper	N/A
pDONR223-GOLGA7	Human Orfeome V7.1	Clone#: 4707385
pCDNA5-GOLGA7-3xFLAG	This paper	N/A
pCDNA5-GOLGA7-C69,72S-3xFLAG	This paper	N/A
Software and Algorithms		
Microsoft Excel	Microsoft Corporation	N/A
Prism 8.0h	GraphPad Software	N/A
ImageJ	Rasband, W.S.	https://imagej.nih.gov/ij/
Morpheus	Broad Institute	https://software.broadinstitute.org/morpheus/

LEAD CONTACT FOR MATERIALS AVAILABILITY

Further information and requests for resources and reagents should be directed to and will be fulfilled by the Lead Contact, Scott Dixon (sjdixon@stanford.edu).

EXPERIMENTAL MODEL AND SUBJECT DETAILS

Cell Lines and Culture Conditions

HT-1080 (sex: male), A549 (sex: male), T98G (sex: male) and HEK 293T (sex: female) cell lines, and control and *Chop*$^{-/-}$ mouse embryonic fibroblasts (MEFs), were obtained from ATCC, expanded for one passage then frozen down in multiple aliquots used for all subsequent experiments. Polyclonal Nuc::mKate2-expressing HT-1080 (HT-1080^{N}), A549^{N}, and T98G^{N} cells were described previously (Forcina et al., 2017). K562 cells transduced with an ultracomplex genome-wide short hairpin RNA library were previously described (Morgens et al., 2016). Control and *ACSL4* gene-disrupted HEK 293 cells were the kind gift of James Olzmann (UC Berkeley), and are described in (Magtanong et al., 2019). Control and *sh-Ripk3* 3T3-SA cells, described in (Mandal et al., 2014), were the kind gift of William Kaiser (UT Health, San Antonio). *Atg5*$^{+/+}$ and *Atg5*$^{-/-}$ MEFs were obtained from the RIKEN BRC Cell Bank (Japan). HAP1 control and *ZDHHC5*^{KO} cell lines were obtained from Horizon Discovery (Cambridge, UK). All cell lines were grown at 37°C with 5% CO_2 in humidified tissue culture incubators (Thermo Scientific, Waltham, MA, USA). HT-1080 cells were grown in Dulbecco's modified Eagle medium (DMEM, Cat# MT-10-013-CV, Thermo Fisher Scientific, Waltham, MA) supplemented with 10% fetal bovine serum

(FBS, Cat# 26140-079, Gibco), 1x non-essential amino acids (NEAAs, Cat# 11140-050, Gibco), and 0.5 U/mL Pen/Strep (P/S, Cat# 15070-063, Gibco). A549, T98G, MEFs, and HEK 293 cells were grown in DMEM, 10% FBS, and 0.5 U/mL P/S. K562 cells were grown in Iscove's modified Dulbecco's medium (IMDM, Cat# SH30228.01, HyClone), 10% FBS, and 0.5 U/mL P/S. HBSS (Cat# 14025-134) and trypsin (Cat# 25200114) used for passaging of adherent cells are from Gibco. For all experiments, cells were counted using a Cellometer Auto T4 cell counter (Nexcelom, Lawrence, MA, USA).

Chemicals and Reagents

CIL56 was synthesized as described (Shimada et al., 2016), or by Acme Bioscience (Palo Alto, CA, USA). Erastin2 corresponds to compound 35MEW28 in (Dixon et al., 2014). Mouse TNFα was the kind gift of J. Carette (Stanford). Dimethyl sulfoxide (Cat# 276855), TOFA (Cat# T6575) staurosporine (Cat# S6942), cycloheximide (Cat# C7698), thapsigargin (Cat# T9033), ferrostatin-1 (Cat# SML0583), brefeldin A (Cat# B7651), and 2-deoxy-D-glucose (Cat# D8375) were from Sigma-Aldrich. Necrostatin-1s (Cat# 2263) was from BioVision (Milpitas, CA). Triacsin C (Cat# 10007448), deferoxamine mesylate (Cat# 14595), carbonyl cyanide-4-(trifluoromethoxy)phenylhydrazone (FCCP, Cat# 15218) and 7BIO (Cat# 19619) were from Cayman Chemicals (Ann Arbor, MI). Bortezomib (Cat# NC0587961) and Q-VD-OPh (Cat# OPH00101M) were obtained from Fisher Scientific. All compounds were prepared as stock solutions in DMSO (Cat# 276855) from Sigma-Aldrich and stored at -20°C until use.

METHOD DETAILS

Cell Line Panel CIL56 Sensitivity Study

The sensitivity of 94 cell lines to CIL56 was tested using the Oncolead service (Karlsfeld, Germany), as follows. All cell lines were tested in parallel in CELLSTAR 96-well microtiter plates (Greiner Bio-One, Germany). Empirically-determined optimal seeding densities were used for each cell line to ensure exponential growth during the course of the experiment. Cells were plated in 90 μL of media and recovered for 48 h before treatment. Stock dilutions of CIL56 in DMSO were prepared in 96-well 0.5 mL MTP plates (Greiner Bio-One). The highest concentration of CIL56 was 25 mM, followed by a 6 point, 7-fold dilution in DMSO, with a lowest concentration of 1.5 μM. The stocks were then diluted 1:100 in RPMI medium. After the 48 h recovery, 10 μL of media containing compound were added to the 90 μL for a final DMSO concentration of 0.1% and high and low doses of 25 μM and 1.5 nM, respectively. Cells were allowed to grow for 72 h before viability quantitation. Parallel plates were also harvested and analyzed after the 48 h recovery period and served as a time zero assessment of cell number. Measurements were performed using a total protein staining protocol. Cells were fixed to the surface by addition of 10% trichloroacetic acid (TCA) (for adherent growing cells) or 50% TCA (for semi-adherent growing cell or cells growing in suspension). After an hour of incubation at 4°C, plates were washed twice with 400 μL of deionized water and dried. Cells were then stained with 100 μL of 0.08% wt/v sulforhodamine B (SRB). The plates were incubated at room temperature for at least 30 min and washed six times with 1% acetic acid to remove unbound stain. The plates were left to dry at room temperature and bound SRB was solubilized with 100 μl of 10 mM Tris base. Optical density was measured at 492, 520, and 560 nm using a Deelux-LED96 plate reader (Deelux Labortechnik GmbH, Germany). Non-linear curve fitting calculations were performed to obtain a dose-response curve for each cell line and IC_{50} values were computed as a 95% confidence interval for a 50% effect of T(compound treated)/C (control).

Cell Death Assessment Using STACK

Where applicable, cell death was assessed using scalable time-lapse analysis of cell death kinetics (STACK) (Forcina et al., 2017). Cell lines stably expressing nuclear-localized mKate2 (Nuc::mKate2) were incubated in medium containing SYTOX Green (Cat# S7020, Life Technologies) at 20 nM. Counts of live ($mKate2^+$) and dead (SG^+) objects were obtained from images obtained every 4 h. The following image extraction parameter values were used to count $mKate2^+$ and/or SG^+ objects: parameter adaptive, threshold adjustment 1; Edge split on; Edge sensitivity 50; Filter area min 20 μm^2, maximum 8100 μm^2; Eccentricity max 1.0; and SG+ objects: Parameter adaptive, threshold adjustment 10; Edge split on; Edge sensitivity -5; Filter area min 20 μm^2, maximum 750 μm^2; Eccentricity max 0.9. Counts were exported to Excel (Microsoft Corp.) and lethal fraction (LF) scores were computed from $mKate2^+$ and SG^+ counts exactly as described (Forcina et al., 2017). For non-$mKate2^+$-marked cells (MEFs, 3T3-SA, HEK 293, and HAP1), the following image extraction parameter values were used to count SG^+ objects: Parameter adaptive, threshold adjustment 1; Edge split on; Edge sensitivity -10; Filter area min 5 μm^2, maximum 800 μm^2; Eccentricity max 0.9.

CIL56 Structure Activity Relationship Analysis

We obtained seven commercial analogs of CIL56 (Sigma Aldrich and ChemDiv, San Diego, CA). Compound were dissolved in DMSO at 10 mM. Cell death was analyzed in HT-1080^N cells. Cells were seeded in 384-well plates at 1,500 cells/well. The next day, cells were treated with CIL56 analogs in a 10-point two-fold dose response, beginning at 10 μM, and cell death was monitored ± TOFA (1 μM) using STACK. The structure of CIL56i [2,7-bis(pyrrolidin-1-ylsulfonyl)-9*H*-fluoren-9-one oxime] was confirmed by the manufacturer, and then again in our lab using liquid chromatography coupled to mass spectrometry (LC-MS). LC-MS was performed with an Agilent Technologies 1260 Infinity attached to a 6120 Quadrupole MS and a Peak Scientific NM32LA nitrogen generator. An Agilent InfinityLab Poroshell 120 EC-C18, 4.6 × 50 mm analytical LC column was used with a flow rate of 0.4 mL/min (solvent A: Milli-Q purified water + 0.1% TFA; solvent B: acetonitrile + 0.1% TFA). CIL56i was dissolved in anhydrous DMSO to a final concentration of 200 μM. 20 μL of CIL56i was injected for a 15-minute gradient of 10%-90% solvent

B into solvent A. CIL56i eluted as a single peak as monitored by UV absorbance at 254 nm and 280 nm using the diode array detector. MS (ESI+, [M+H]), 462.2.

Genome-wide shRNA Screen

Genome-wide short hairpin RNA (shRNA) screening was performed in K562 cells transduced with an ultracomplex (average 25 shRNA/gene) library as previously described (Morgens et al., 2016). Cells were maintained at between $5x10^8$ and $1x10^9$ cells in 1 L media in spinner flasks to ensure both log-phase growth and roughly 1,000-fold coverage. For the screen, $5x10^8$ cells were thawed into 600 mL of medium in one flask. Then the next day the cells were counted and the total volume of medium was raised to 1 L. The day after that, cells were counted, split into two flasks to give a total of $5x10^8$ cells in a final volume of 1 L of medium in each flask and cells were treated with either 1.25 μM CIL56 or 1.25 μM CIL56i for 24 h. Then, cells were counted, pelleted by centrifugation, and resuspended to a concentration of $5x10^8$ cells/L in fresh medium. This selection was repeated three more times over 12 d. Next, cells were pelleted and genomic DNA extracted with QIAamp DNA Blood Maxi Kit (Qiagen). shRNA library preparation was done as previously described (Deans et al., 2016) with two rounds of PCR with Agilent Herculase II Fusion DNA Polymerase (Agilent, Santa Clara, CA). shRNA-encoding constructs were analyzed by deep sequencing on an Illumina Nextseq. The sequencing results were analyzed as previously described (Deans et al., 2016). Briefly, a maximum likelihood estimator (MLE) was developed to approximate the maximum effect size of the set of shRNAs targeting each gene. The distribution of shRNAs for a given gene was fit to a mixed model with three distributions: off-target, miss, and on-target. Estimations for off-target and missed distributions were performed by Gaussian kernel smoother with the bandwidth determined by Scotts' rule. On-target distribution was the uniform distribution from 0 to I, where I is a fitted parameter and corresponds to the estimated effect size. The relative contribution of the missed and on-target distribution was fitted, allowing for different numbers of shRNAs to be considered on-target, and the contribution of the off-target distribution was fixed at 10% to allow for outliers. Significance of the MLE was tested using a log-likelihood ratio, with *p*-values empirically determined by repeated sampling of all shRNAs. Enrichment values for each shRNA were calculated as the log ratio of the frequency of the shRNA in control and CIL56-treated samples. For each gene, the MLE was used to estimate the effect of the entire set of shRNAs targeting that gene, and a *p*-value representing the significance of that effect (casTLE score). Genes were then filtered by significance under the Bonferroni correction at $p < 0.05$ and ranked according to the estimated effect size (casTLE effect).

CRISPR/Cas9 Gene Editing

HT-1080, HT-1080^N, $A549^N$, and HEK 293T cells lacking ZDHHC5, GOLGA7, or ZDHHC9 were generated as follows. The sgRNA primer sets ZDHHC5 sg1, ZDHHC9 sg1, and GOLGA7 sg2 (Table S1) were used. sgRNAs were cloned into pSpCas9(BB)-2A-GFP (a kind gift from Dr. Jan Carette (Stanford University School of Medicine), described in (Ran et al., 2013)). Briefly, a mixture of 1 μL of each sgRNA primer set (100 μM) plus 8 μL of ddH2O was prepared, heated to 95°C, then cooled at a rate of 2.5°C/minute to 25°C. The oligo duplex was then diluted 1:200 in ddH2O and used for cloning into pSD224, the pSpCas9(BB) plasmid. The ligation reaction was: 100 ng pSD224, 2 μL of the diluted oligo duplex, 2 μL of 10x FastDigest buffer (Thermo Scientific), 1 μL 10 mM DTT, 1 μL 10 mM ATP, 1 μL FastDigest BpiI (Cat# D1014, Thermo Scientific), 0.5 μL T4 DNA ligase (Cat# EL0014, Thermo Scientific), and completed to 20 μL with ddH2O. The ligation reaction was incubated for 1 hour [(37°C, 5 min; 21°C, 5 min) x 6 cycles]. 2 μL of the ligation product was used to transform competent DH5α. Transformants were selected on LB+amp (100 μg/mL). Plasmid DNA was extracted using a QIAGEN spin column (Cat# 27106, QIAGEN, Hilden, Germany) and sent for sequencing. Cells were transfected with 2.5 μg DNA using Opti-MEM I Reduced Serum Medium (Cat# 31985-062, Life Technologies) and Lipofectamine LTX Reagent with PLUS Reagent (Cat# 15338-100, Life Technologies), according to the manufacturer's instructions. Cells were allowed to recover for 24 h in fresh media, and the following day, GFP+ cells were single-sorted using a BD FACSJazz Cell Sorter (BD Biosciences) (Stanford Shared FACS Facility) into a 96-well plate containing either DMEM containing 30% FBS and 0.5 U/mL P/S (for HEK 293T and $A549^N$ cells) or DMEM containing 1x NEAAs, 30% FBS, and 0.5 U/mL P/S (for HT-1080 and HT-1080^N cells). Cells were incubated at 37°C until distinct clones appeared. Individual clones were amplified in normal (10% FBS) medium to produce enough cells for gDNA extraction and protein lysis. gDNA extraction was performed using a NucleoSpin Tissue column (Cat# 740952, Takara Bio). 50-100 ng of gDNA was used as PCR template to amplify a region of DNA flanking the sgRNA recognition site. Amplicons were generated using primers listed in Table S1 and the PCR product was purified using a QIAGEN PCR Purification column (Cat# 28106) and sent for sequencing using the sequencing primers listed in Table S1. Clones with frame-shift mutations in the regions of interest were confirmed by Western blot (see below) for loss of protein expression.

ZDHHC and GOLGA7 Biochemistry

cDNA from human GOLGA7 (Genbank Accession #CV025062) in a pDONR223 vector was obtained from the human ORFeome V7.1 library (clone ID 4707385, a kind gift of Dr. Aaron Gitler). The cDNA was cloned into a pDEST-pCDNA-FLAG C-term, a kind gift of Dr. Anne-Claude Gingras (Couzens et al., 2013). The $GOLGA7^{2CS}$ mutant was generated using the Q5 Site-directed mutagenesis Kit (Cat# E0554, New England BioLabs), using the *GOLGA7-C69,72A* primer set (Table S1). Control pEF-BOS-HA, pEF-BOS-HA-Zdhhc5 (NM_144887), pEF-BOS-HA-Zdhhc9 (AK032233), pEF-BOS-HA-Zdhhc2 (NM_178395), and pEF-BOS-HA-Zdhhc8 (AY668947) were a kind gift of Dr. Masaki Fukata. The $Zdhhc5^{DHHS}$ and $Zdhhc5^{3CS}$ mutants were generated using the Q5 site-directed mutagenesis kit (New England Biolabs) using the *ZDHHC5-C134S* and *ZDHHC5-C236,237,245S* primer sets (Table S1). The $Zdhhc5^{3YA}$ mutant was generated using the Q5 site-directed mutagenesis kit and each of the *ZDHHC5-Y456A*, *ZDHHC5-Y470A*, and *ZDHHC5-Y533A*

primer sets sequentially (Table S1). For expression and coimmunoprecipitation studies, 600,000 HEK293T cells were seeded in 6-well plates 24 h prior to transfection. Cells were transfected with Lipofectamine LTX Reagent with PLUS Reagent and OPTI-MEM I Reduced Serum Medium according to the manufacturer's instructions with 2.5 μg DNA per well. Cells were washed and collected in ice-cold HBSS. The pelleted cells were stored at -80°C until lysis. Cells were solubilized in TNE (50 mM Tris, pH 7.4, 150 mM sodium chloride, and 2 mM EDTA) containing 1% *n*-dodecyl-β-maltoside (Cat# 89902, Thermo Fisher Scientific) and protease inhibitor cocktail (Cat# P8340, Sigma-Aldrich) using a 25-gauge needle syringe. Lysates were cleared by spinning for 16,000xg for 15 min at 4°C and diluted 1:1 with TNE containing no detergent (final *n*-dodecyl-β-maltoside concentration of 0.5%). Protein levels were quantitated with Pierce BCA Protein assay (Thermo Fisher Scientific). For the coimmunoprecipitation, 30 μg of lysate was set aside for input. Lysate was added to pre-washed Anti-FLAG(R) M2 Magnetic Beads (Sigma-Aldrich) at 1 mg/mL in 300 μL and incubated at 4°C for 2 h with end-over-end rotation. Beads were washed three times with TNE containing 0.5% *n*-dodecyl-β-maltoside before elution directly into Bolt LDS Sample Buffer (Life Technologies). Elution was carried out by vortexing for 5 min at 4°C followed by incubating for 8 min at 80°C. Immunoprecipitated proteins were analyzed by immunoblotting (details below).

Immunoblotting

Adherent cells were washed twice in PBS and harvested using a cell scraper. Cells were spun down (1,000 x g, 1 min) and the supernatant removed and discarded. Cell pellets were immediately stored at -80°C until lysis. Cell pellets were homogenized and lysed in RIPA buffer (50 mM Tris pH 7.5, 150mM NaCl, 0.5% NP-40, 0.1% Sodium deoxycolate, 1% Triton X-100, 0.1% SDS, 2 mM EDTA). Lysates were spun down (18,000 x g, 15 min, 4°C) to remove un-lysed cells and debris. Protein levels were quantitated with Pierce BCA Protein assay (Thermo Fisher Scientific). Equal amounts of protein were combined with 4x Bolt LDS Sample Buffer (Cat# B0007) and 10x Bolt Sample Reducing Agent (Cat# B0009, Life Technologies) and loaded onto a Bolt 4-12% Bis-Tris Plus Gel (Cat# NW04120BOX, Life Technologies). Protein was transferred to a nitrocellulose membrane using an iBlot2 transfer stack (Life Technologies). The membrane was blocked using Odyssey Blocking Buffer (Cat# 927-50000, LI-COR Biotechnology, Lincoln, NE) (1 h, RT) and incubated in primary antibody mixture (overnight, 4°C). Primary antibodies used were goat α-actin (Cat# sc-1616, Santa Cruz Biotechnology, Dallas, TX; 1:2000), mouse α-actin (Cat# sc-47778, Santa Cruz Biotechnology, 1:1000), rabbit α-ZDHHC5 (Cat# HPA014670, Sigma-Aldrich, 1:250), mouse α-GOLGA7 (Cat# H00051125, Novus Biologicals, 1:250), rabbit α-ZDHHC9 (Cat# NBP1-84499, Novus Biologicals, 1:250), mouse α-tubulin (Cat# MS581P, Fisher Scientific, 1:10,000), goat α-FLAG (Cat# ab1257, Abcam, 1:15,000), rabbit α-HA (Cat# 3724S, Cell Signaling Technology), and mouse α-HA (Cat# 901502, BioLegend, 1:15,000). Membranes were washed three times in Tris buffered saline (Cat # 0788, ISC BioExpress) with 0.1% Tween 20 (TBST), then incubated with secondary antibody mixture (1 h, room temperature). Secondary antibodies used were donkey α-rabbit (Cat# 926-32213, 926-68023, LI-COR Biotechnology, Lincoln, NE, 1:15,000 dilution), donkey α-goat (Cat# 926-32214, 926-68024, LI-COR Biotechnology, 1:15,000 dilution), and donkey α-mouse (Cat# 926-32212, 926-68022, LI-COR Biotechnology, 1:15,000 dilution) in Odyssey Blocking Buffer. The membrane was washed 3 times in TBST and then scanned on an Odyssey CLx Imaging System (LI-COR Biotechnology).

Acyl Resin-Assisted Capture

Acyl resin-assisted capture (Acyl-RAC) was performed as follows. $1.5x10^6$ 293T cells were seeded in a 10 cm plate for 24 h before transfection. Cells were transfected with 15 μg DNA with Lipofectamine LTX Reagent with PLUS Reagent and OPTI-MEM I Reduced Serum Medium according to manufacturer instructions. Transfected cell pellets were harvested and stored at -80°C until lysis. The resulting cell pellet was resuspended in 500 μL lysis buffer (25 mM HEPES [pH 7.4], 25 mM NaCl, 1 mM EDTA, Protease Inhibitor Cocktail P8340 (Sigma-Aldrich)). The cell suspension was snap-frozen in liquid nitrogen and thawed at 37°C for 5 min three times. Lysis was completed by passing suspension through a 25-gauge needle syringe. The crude cell lysate was centrifuged (800×g, 5 min, 4°C) to remove nuclear debris and unbroken cells. The resultant supernatant was transferred to ultracentrifuge tubes (Cat# 343776 Beckman-Coulter) and centrifuged (100,000×g, 1 hr, 4°C) in an OptimaTLX Ultracentrifuge (Beckman-Coulter) to pellet the membrane fraction. The resulting pellet was resuspended in blocking buffer (100 mM HEPES [pH 7.5], 1 mM EDTA, 1% SDS, N-ethyl-maleimide (Cat# 40526, Alfa Aesar, Ward Hill, MA)). Protein concentration was measured by a BCA assay-kit according to the manual (Pierce) and diluted to 4 mg/mL with additional blocking buffer. Blocking took place at 40°C for 2 h with gentle agitation and was followed by adding 1.6 mL ice-cold acetone and storing overnight at -20°C to precipitate the protein. The precipitated proteins were centrifuged (13,000×g, 15 min, 4°C) and washed three times with 70% acetone/water. The final pellet was air-dried, resuspended in 400 μL binding buffer (100 mM HEPES [pH 7.5], 1 mM EDTA, 1% SDS), and incubated at 30°C for 2 h. 40 μL of the suspension was set aside as input. The remaining suspension was split in half and added to 50 μg activated thiopropyl sepharose 6B (GE Healthcare) suspended in binding buffer. One part was treated with 0.5 M hydroxylamine [pH 7.5] for thioester cleavage; the other part with 0.5 M NaCl solution as a negative control. The bead slurry was incubated on an end-over-end shaker at 30°C overnight. The next day, the beads were washed five times with binding buffer and centrifuged at 1000×g, for 1 min. The bound protein was eluted into 80 μL of binding buffer with 150 mM DTT and incubation for 30 min with gentle agitation. 20 μL of sample buffer was added to eluted protein and incubated at 95°C for 15 min. 50 μL of the resultant sample was loaded onto SDS-PAGE gel for Western blot analysis.

Confocal Immunofluorescence Imaging

40,000 HT-1080 cells were seeded on #1.5 glass coverslips in a 12-well plate 24 h prior to transfection (see specific sections below for additional details). To improve cell viability and transfection efficiency, cells for transfection were seeded on coverslips coated with poly-D-lysine. Where applicable, cells were transfected as described above with 0.5 μg DNA with Lipofectamine LTX Reagent with

PLUS Reagent (Invitrogen) 24 h before drug treatment(s). Treated coverslips were rinsed in 1x PBS and fixed in 4% paraformaldehyde (Alfa Aesar) for 20 min at room temperature. Cells were rinsed once with 1x PBS and permeabilized overnight at 4°C in 1x PBS with 3% BSA (Gemini Bio Products, West Sacramento, CA), 0.1% Triton X-100, and 0.02% sodium azide (PBS-BT). Coverslips were transferred to hydration chamber and covered in 30 μL PBS-BT. 30 μL primary antibody mix was applied to coverslips for 1 h at room temperature. Primary antibodies used were rabbit α-ZDHHC5 (Cat# HPA014670, Sigma-Aldrich, 1:100), goat α-FLAG (Cat# ab1257, Abcam, 1:1000), mouse α-HA (Cat# 901502, BioLegend, 1:1000), mouse α-GM130 (BD Biosciences, 1:500), rabbit α-TGN46 (Cat# NBP1-49643, Novus Biologicals, 1:100), rabbit α-EGFR (Cat# D38B1, Cell Signaling Technology, 1:100) and mouse α-CD71 (Cat# BE0023, BioXCell, 1:100). Coverslips were washed 3 times with PBS-BT and incubated with 30 μL of the appropriate secondary antibody mix (1:1000 of each secondary antibody, obtained from Life Technologies) for 1 h at room temperature. Secondary antibodies used were goat α-rabbit (Cat# A11036, Life Technologies), goat α-mouse (Cat# A11029, Life Technologies), donkey α-goat (Cat# A11057, Life Technologies), and donkey α-rabbit (Cat# A21206, Life Technologies). All secondary antibodies were used at 1:1000. Coverslips were washed three times with PBS-BT and incubated with 20 μL DAPI (Cat# D1306 Thermo Fisher) at 0.1 μg/mL for 20 min. Coverslips were washed five more times with PBS-BT and then mounted in ProLong Gold antifade reagent (Cat# P10144, Thermo Fisher). Coverslips were cured overnight at room temperature in the dark before imaging. Confocal images were obtained on a Zeiss Axio Observer microscope (Carl Zeiss) with a confocal spinning-disk head (Yokogawa Electric Corporation, Tokyo, Japan), PlanApoChromat 63×/1.4 NA objective, and a Cascade II:512 electron-multiplying (EM) CCD camera (Photometrics, Tucson, AZ). Images shown in Figures 3G, 4B, 4D, 4E, S3D, S4C, and S4D are composite images generated using ImageJ.

Transmission Electron Microscopy

Control and *ZDHHC5*^{KO1} HT-1080 cells were seeded on #1.5 glass coverslips (Electron Microscopy Sciences) 24 h prior to treatment. Cells were treated with either DMSO or 2.5 μM CIL56 for 4 h. Cells were rinsed with PBS twice and incubated in 2.5% glutaraldehyde for 1 h at room temperature. The coverslips were then rinsed another three times in PBS before storing in PBS. Sample dehydration, embedding, sectioning, and transmission electron microscopy were performed at the University of Pittsburg Center for Biologic Imaging. Briefly, coverslips were dehydrated in graded series of ethanol (30%, 50%, 70%, and 90%) for 10 min followed by three 15 min changes in 100% ethanol. Dehydrated coverslips were then changed in Epon three times for 1 h each. Beam capsules full of resin were inverted over coverslips and polymerized at 37°C overnight followed by 60°C for 48 h and sectioning. Images were acquired with a JEM-1400 Plus Transmission Electron Microscope (JEOL USA, Peabody, MA) and an XR611 camera (Advanced Microscopy Techniques, Woburn, MA).

Mitochondria and ER Morphological and Functional Assessment

To examine the mitochondrial network in live cells, 40,000 HT-1080^{N} cells were seeded in a 12-well plate the day before transfection. Cells were transfected with Lipofectamine LTX Reagent with PLUS Reagent (Invitrogen) 24 h before drug treatment(s) according to manufacturer instructions with 0.5 μg pmTurquoise2-Mito plasmid. pmTurquoise2-Mito was a gift from Dorus Gadella (Addgene #36208; RRID:Addgene_36208; (Goedhart et al., 2012)). Control and *ZDHHC5*^{KO1} cells were treated with DMSO, CIL56 (2.5 μM, 4 h) or FCCP (10 μM, 30 min) prior to imaging. Cells were imaged using the Lionheart FX Automated Microscope (BioTek) with a Plan Fluorite 40x/0.6 NA objective (PN 1220544, BioTek) and a 16-bit grayscale Sony CMOS camera. GFP and Texas-Red filter cubes (PN 1225101, PN 1225102, BioTek) were used to acquire images. Images shown in Figure S4B are composite images generated using ImageJ. To examine the morphology of the endoplasmic reticulum (ER) in live cells, 80,000 HT-1080^{N} cells were seeded on #1.5 glass coverslips in a 6-well plate 24 h before the experiment. Cells were transfected with Lipofectamine LTX Reagent with PLUS Reagent (Invitrogen) 24 h before drug treatment(s) according to manufacturer instructions with 0.5 μg pmTurquoise2-ER plasmid. pmTurquoise2-ER was a gift from Dorus Gadella (Addgene #36204; RRID: Addgene_36204; (Goedhart et al., 2012)). The next day, cells were treated for 4 h with DMSO or CIL56 (10 μM), rinsed once with HBSS and inverted onto glass slides with 20 μL HBSS. Samples were imaged on a spinning-disk confocal microscope (see confocal imaging details above).

Cellular ATP levels were measured using CellTiter-Glo reagent (Cat# G7572, Promega). HT-1080 cells were seeded at a density of 1,500 cells/well of a 384-well plate. The next day, cells were treated with vehicle (DMSO), CIL56 (10 μM), or a positive control inhibitor of glycolysis, (2-deoxy-D-glucose, 50 mM) for 6 h. Then, 40 μL of CellTiter-Glo reagent (Promega) was added to each well and mixed for 2 min on an orbital shaker and incubated at RT for 10 min. Luminescence was measured using a Cytation3 multimode plate reader (BioTek, Winooski, VT, USA) from the top with the gain set to 135. ATP values in the treated conditions are expressed as a fraction of the DMSO control values. Cellular oxygen consumption and extracellular acidification was analyzed using a Seahorse instrument. A549^{N} cells were seeded at 10,000 cells/well into Seahorse XFp cell culture miniplates in a final volume of 80 μL, briefly spun at 500 rpm, and allowed to settle overnight at 37°C and 5% CO_2. 200 μL of XF calibrant (pH 7.4) was added to an XFp extracellular flux cartridge and left at 37°C in the absence of CO_2. The next day, cells were washed twice with 200 μL of Seahorse medium (XF Base Medium Minimal DMEM, 25 mM glucose, 1.0 mM sodium pyruvate, 4 mM glutamine, pH 7.4). After washing, each well was incubated in 180 μL Seahorse medium. At this point, the wells were imaged using the IncuCyte to obtain mKate2+ live cell counts that were used for normalization. The cell culture miniplate was allowed to incubate at 37°C in the absence of CO_2 for one hour prior to the beginning of the experiment. Compounds were prepared at 10x in Seahorse medium in a final volume of 20 μL in the XFp extracellular flux cartridge to be injected later in the experiment. Oxygen consumption rate (OCR) and extracellular acidification rate (ECAR) were monitored 25 min pre-compound injection and for 240 min post-compound

injection (CIL56 final concentration = 10 μM). Mitochondrial inner membrane transmembrane potential was imaged with JC-1 dye (Cat# T3168, Thermo Fisher Scientific). 125,000 HT-1080 cells were seeded on #1.5 glass coverslips in a 6-well plate 24 h before the experiment. Cells were treated with DMSO, 2.5 μM CIL56 for 4 h, or 10 μM FCCP for 30 minutes. Cells were labeled with 1 mL of HBSS containing 10 μg/mL JC-1 dye and 1 μg/mL Hoechst (Cat# H1399, Molecular Probes) for 10 min. Coverslips were rinsed three times with 1 mL HBSS and inverted onto glass slides with 20 μL HBSS. Samples were imaged on a spinning-disk confocal microscope as described above.

Golgi Imaging and RUSH Analysis

To image *trans*- and *cis*-Golgi compartments, 80,000 HT-1080 cells were seeded on #1.5 glass coverslips in a 12-well plate 24 h before the experiment. Cells were treated with 2.5 μM CIL56 for 4 h. Cell fixation, antibody labeling, and sample imaging was carried out according to the confocal imaging details above. Image processing and quantification of the *trans*- and *cis*-Golgi compartments were carried out as follows using ImageJ. Images were background-subtracted using a rolling ball radius of 50 pixels. Then, for each cell, the total area of green (*cis*) and red (*trans*) signal above threshold was measured. For live cell imaging, 80,000 HT-1080^{N} cells were seeded on #1.5 glass coverslips in a 6-well plate 24 h before the experiment. Cells were transfected with Lipofectamine LTX Reagent with PLUS Reagent (Invitrogen) 24 h before drug treatment(s) according to manufacturer instructions with 0.5 μg eYFP-β-galactosyltransferase (EYFP-Golgi-7) plasmid. EYFP-Golgi-7 was a gift from Michael Davidson (Addgene #56590; RRID: Addgene_56590; (Olenych et al., 2007)). The next day, cells were treated with 10 μM CIL56 for 0, 0.5, 1, 2, 4, or 6 h, rinsed once with HBSS and inverted onto glass slides with 20 μL HBSS. Samples were imaged on a spinning-disk confocal microscope (see microscope details above).

For RUSH analysis, Control or *ZDHHC5*^{KO1} cells were examined in separate experiments on different days. In both cases, 40,000 HT-1080 were seeded in a 12-well plate the day before transfection. Cells were transfected with Lipofectamine LTX Reagent with PLUS Reagent (Invitrogen) 24 h before drug treatment(s) according to manufacturer instructions with 0.5 μg Str-KDEL_TNF-SBP-EGFP. The Str-KDEL_TNF-SBP-EGFP plasmid was a gift from Franck Perez (Addgene #65278; RRID:Addgene_65278; (Boncompain et al., 2012)). The next day, the media was aspirated and 0.5 mL of DMEM containing no phenol red (Cat# 21063-029, Gibco) supplemented with 10% FBS was added to each well. The assay plate was placed in the Lionheart for image acquisition (details above) and the automated acquisition was initiated prior to addition of biotin (Cat# B40040, Research Products International) and CIL56. Images were acquired every 5 min (Control) or 10 min (*ZDHHC5*^{KO1}). In between acquisitions, 0.5 mL of media lacking phenol red with 80 μM biotin ± 5 μM CIL56 was added to each well (final concentrations = 40 μM biotin, 2.5 μM CIL56). Quantification of RUSH dynamics was carried out as follows. For each cell measured, fluorescence intensity threshold was determined empirically based on the visible formation of Golgi structure. After thresholding, fluorescence intensity was measured throughout the entire time course. The time point with maximum integrated density (maximum Golgi signal) was considered time zero and set equal to an arbitrary value of 1. Data normalization was done by dividing the integrated density at each time point by the maximum integrated density (time zero) to obtain the fraction of signal present. These values were graphed on a log scale to reflect the fraction of the maximum signal present over the treatment time course before and after the time of maximum intensity.

RNA Sequencing Analysis

Control and *ZDHHC5*^{KO} HEK 293T cells were seeded in 6-well plates at 600,000 cells per well 24 hours before treatment. Wells were treated in duplicate with either 2.5 μM CIL56 or DMSO for 1 h before harvesting and pelleting in cold HBSS and snap freezing on dry ice. Cell pellets were stored at -80°C until RNA extraction. Cell pellets were lysed and RNA extracted with Qiashredder and RNeasy Plus mini Kits (Cat# 796554, 74134, Qiagen) in duplicate according to manufacturer's instructions. RNA purity, integrity, and concentration were quantified at the Stanford Protein and Nucleic Acid Facility by NanoDrop Spectrophotomer (Thermo Fisher Scientific) and by Eukaryote Total RNA Nano chip analysis on a 2100 Bioanalyzer (Agilent). By Bioanalyzer, the RNA Integrity Number for each sample met a threshold of at least 6.8, and NanoDrop 260/280 and 260/230 ratios met a threshold of at least 1.95. RNA samples were sent to Novogene (Sacramento, CA) for library generation, 20M read PE150 sequencing on an Illumina HiSeq 4000 platform, and bioinformatics analysis. Reads with adaptor contamination, >10% uncertain nucleotides, or >50% nucleotides with base quality <20 were filtered out, and the remaining clean reads (at least 94% of reads in all conditions) were aligned to the reference genome using Tophat v2.0.12. At least 93% of clean reads were successfully mapped in all conditions. Pearson correlations between biological replicates yielded R^2 values above 0.98 in all conditions. Differentially expressed genes were identified using DESeq 1.10.1. Only genes with FKPM counts > 1 and altered by more than 2-fold in CIL56 versus DMSO-treated Control condition are shown in Figure S4A. Data were plotted using Morpheus (https://software.broadinstitute.org/morpheus/).

QUANTIFICATION AND STATISTICAL ANALYSIS

Where appropriate, lethal fraction scoring were performed using Excel 14.6.0 as described (Forcina et al., 2017). Images acquired on the IncuCyte were processed and analyzed with the Zoom software package (v2016A/B). Images acquired on the spinning disk confocal were processed analyzed with ImageJ. Images acquired on the Lionheart FX (BioTek) were processed and analyzed with Gen5 software and ImageJ v1.8.0 (US National Institutes of Health, Bethesda, MD). Graphing and all other statistical analyses were performed using Prism 8. Figures were assembled using Adobe Illustrator. Except where noted, all data represent mean ± standard deviation (SD) of three biological replicates.

DATA AND CODE AVAILABILITY

RNA sequencing data for 293T Control and ZDHHC5^{KO} cells treated ± CIL56 (2.5 μM, 1 h) are available online via the Mendeley Data repository at https://data.mendeley.com/datasets/m6fp39vyd9/1.